Symmetric Achromatic Variability in Active Galaxies: A Powerful New Gravitational Lensing Probe?

H. K. Vedantham[1], A. C. S. Readhead[1], T. Hovatta[2,3,4], T. J. Pearson[1], R. D. Blandford[5], M. A. Gurwell[6], A. Lähteenmäki[2], W. Max-Moerbeck[7], V. Pavlidou[8], V. Ravi[1], R. A. Reeves[9], J. L. Richards[1], M. Tornikoski[2], and J. A. Zensus[7]

[1] Owens Valley Radio Observatory, California Institute of Technology, Pasadena, CA 91125, USA
[2] Aalto University Metsähovi Radio Observatory, Metsähovintie 114, FI-02540 Kylmälä, Finland
[3] Aalto University Department of Radio Science and Engineering, Finland
[4] Tuorla Observatory, Department of Physics and Astronomy, University of Turku, Finland
[5] Kavli Institute for Particle Astrophysics and Cosmology, Department of Physics, and SLAC National Accelerator Laboratory, Stanford University, Stanford, CA 94305, USA
[6] Harvard-Smithsonian Center for Astrophysics, Cambridge, MA 02138, USA
[7] Max-Planck-Institut für Radioastronomie, Auf dem Hügel 69, D-53121 Bonn, Germany
[8] Department of Physics and Institute of Theoretical and Computational Physics, University of Crete, 71003 Heraklion, Greece
and Foundation for Research and Technology—Hellas, IESL, 7110 Heraklion, Greece
[9] CePIA, Astronomy Department, Universidad de Concepción, Casilla 160-C, Concepción, Chile

Abstract

We report the discovery of a rare new form of long-term radio variability in the light curves of active galaxies (AG) —symmetric achromatic variability (SAV)—a pair of opposed and strongly skewed peaks in the radio flux density observed over a broad frequency range. We propose that SAV arises through gravitational milli-lensing when relativistically moving features in AG jets move through gravitational lensing caustics created by 10^3–$10^6\,M_\odot$ subhalo condensates or black holes located within intervening galaxies. The lower end of this mass range has been inaccessible with previous gravitational lensing techniques. This new interpretation of some AG variability can easily be tested and if it passes these tests, will enable a new and powerful probe of cosmological matter distribution on these intermediate-mass scales, as well as provide, for the first time, micro-arcsecond resolution of the nuclei of AG—a factor of 30–100 greater resolution than is possible with ground-based millimeter very-long-baseline interferometry.

Key words: BL Lacertae objects: individual (J1415+1320) – gravitational lensing: strong – radio continuum: galaxies

1. Introduction

We report a hitherto unrecognized form of radio variability in active galaxies (AG)—symmetric achromatic variability (SAV)—which is time-symmetric and achromatic from 15 to 234 GHz.[10] SAV was first noticed in an unusual year-long symmetric U-shaped feature that appeared in the 15 GHz light curve of the BL Lac object J1415+1320 (PKS 1413+135), in 2009–2010 (see Figure 1). The radio source lies either within or behind a spiral galaxy at redshift $z = 0.247$ (Beichman et al. 1981; McHardy et al. 1991; Carilli et al. 1992). The U-shaped symmetry is similar to that observed in extreme scattering events (ESEs; Fiedler et al. 1987; Pushkarev et al. 2013) caused by interstellar plasma structures, but the achromaticity, among other factors, can be shown to rule out ESEs as the origin of SAV (Vedantham et al. 2017). A pair of forward–reverse shocks within the source may create achromatic U-shaped events (Kobayashi & Zhang 2003), but these are not expected to yield the high degree of symmetry observed in J1415+1320.

We propose that SAV is caused by the modulation of the flux density of a luminal or superluminal (Begelman et al. 1984) compact emission region as it traverses the magnification pattern cast by an intervening gravitational lens. The proposed lensing mechanism is akin to microlensing of stars by stellar-mass lenses (Alcock et al. 1993), but the lenses would need to

be in the milli-lensing mass range $\sim 10^3$–$10^6\,M_\odot$, with a projected surface mass density of $\gtrsim 10^4\,M_\odot\,{\rm pc}^{-2}$. Potential lens candidates with these properties include the dense cores of globular clusters and molecular clouds, and massive black holes. The lenses likely consist of multiple components that are projected close to the line of sight to the source, but are not necessarily gravitationally bound to each other.

The intermediate-mass range has not been accessible by traditional centimeter-wavelength very-long-baseline interferometry (VLBI) searches for multiple images (Wilkinson et al. 2001) or time delays (Fassnacht et al. 1999), and although the upper half of this mass range is now being probed by millimeter wavelength VLBI (Marscher & Jorstad 2010; Brinkerink et al. 2016), the lower half is still barely within reach. SAV may thus provide a powerful new method of exploiting gravitational lensing in addition to the two traditional methods employing multiple images and time delays. We note that our gravitational milli-lensing hypothesis leads to a number of testable predictions and is correspondingly fragile. We regard this as a strength of the hypothesis—it should be easy to disprove.

The paper is organized as follows. Section 2 describes the Owens Valley Radio Observatory (OVRO) blazar monitoring survey in which SAV was first identified, and presents observational details of multifrequency radio light curves of J1415+1320. Section 3 describes the SAV observed in J1415 +1320 and the rate of U-shaped events in the OVRO survey. In Section 4 we summarize the known radio and optical properties

---

[10] We use "SAV" to denote symmetric achromatic variability, symmetric achromatic variations, and symmetric achromatic variable, relying on the context to make the usage clear.
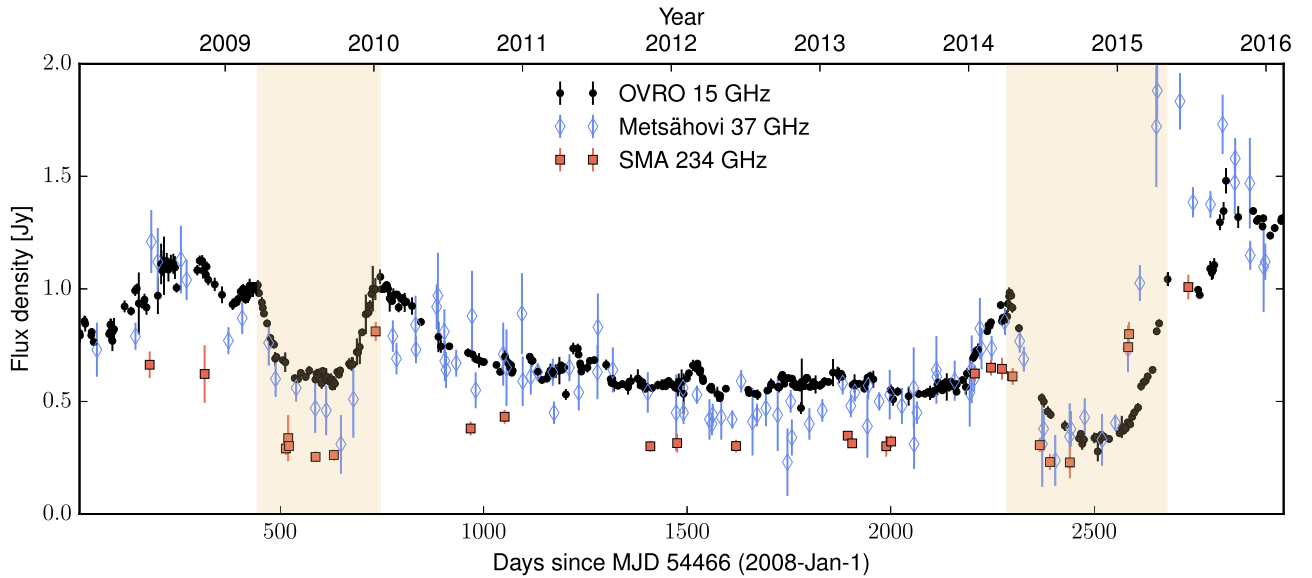
Figure 1. Multifrequency light curves of J1415+1320 showing symmetric achromatic variability (SAV). The roughly 1-year-long U-shaped SAV events in 2009 and 2014 are highlighted.

of J1415+1320. In Section 5 we present simple lens models that can account for the observed SAV features in J1415+1320 as an "existence proof." Though the light curves cannot be inverted to obtain a unique lens model, we exploit some generic properties of gravitational lenses to place constraints on the lens mass and projected surface density. Finally, in Section 6, we discuss the general and J1415+1320-specific implications of the lensing hypothesis, and make falsifiable predictions to test the lensing hypothesis.

2. The Observations

We report here on four series of radio flux density-monitoring observations, carried out at 15 GHz on the 40 m telescope at OVRO, at 22 and 37 GHz on the 13.7 m telescope of the Metsähovi Radio Observatory (MRO), at 100 GHz on the 6 × 10.4 m OVRO millimeter array, and at 234 GHz on the 8 × 6 m Sub-Millimeter Array (SMA) of the Smithsonian Astrophysical Observatory (SAO).

2.1. OVRO 15 GHz

2.1.1. The Sample

Since 2008 the OVRO 40 m telescope blazar monitoring survey has accumulated ∼12,000 object-years of observations and is by far the largest and most sensitive radio monitoring survey of blazars undertaken thus far. The survey is being carried out in support of the *Fermi* Gamma-Ray Space Telescope and the sample comprises mostly candidate gamma-ray blazars. This program started as a survey of 15 GHz radio variability of a complete sample of 1158 AG (Richards et al. 2011), which has been augmented by the addition of several hundred *Fermi*-detected blazars that are not in the original sample, samples of galactic micro-quasars, NLS1 galaxies, and the sample of sources detected at TeV energies,[11] so that our whole sample now contains ∼1830 objects each observed about twice per week, hardware problems and weather permitting.

The complete sample comprising 1158 objects was selected from a uniform all-sky survey of bright quasars in the Candidate Gamma-Ray Blazar Survey (CGRaBS; Healey et al. 2008). The CGRaBS sample was selected from objects in the Cosmic Lens All Sky Survey (Myers et al. 2003), together with observations at both 4.8 and 8.4 GHz. Over 11,000 objects brighter than 65 mJy at 4.8 GHz, and with spectral index $\alpha > -0.5$ ($S \propto \nu^{\alpha}$) were selected initially. Since the 40 m program is in support of *Fermi*-GST, we restricted the sample to EGRET-like blazars (Hartman et al. 1999; Mattox et al. 2001), and thus applied a figure of merit based on 3EG blazar objects in CLASS, which yielded 1625 objects, of which 1158 have declinations $>-20°$ and can be monitored by the 40 m telescope. We concentrate here on this statistically complete sample, in which we find that 981 objects have a high enough signal-to-noise ratio to identify symmetrical U-shaped features in their light curves.

2.1.2. The Observations

The 15 GHz observations were made with the 40 m telescope of the OVRO in California (37°.2314 N, 118°.2827 W). The 40 m telescope uses off-axis dual-beam optics and a cryogenic receiver with a 15 GHz center frequency and 3 GHz bandwidth. The two sky beams are Dicke-switched using the off-source beam as a reference. The source is alternated between the two beams in an ON–ON fashion to remove atmospheric and ground contamination. The on-source observing time is 32 s and the 3σ detection limit is 12 mJy in good weather.

In 2014 May, a new pseudo-correlation receiver was installed on the 40 m telescope, and the gain variations have since been corrected using a 180° phase switch instead of a Dicke switch. The performance of the new receiver is very similar to the old one and no discontinuity is seen in the light curves. Calibration is achieved using a temperature-stable diode noise source to remove receiver gain drifts, and the flux density scale is derived from observations of 3C 286 assuming a value of 3.44 Jy at 15 GHz (Baars et al. 1977). The systematic uncertainty of about 5% in the flux density scale is not included

---
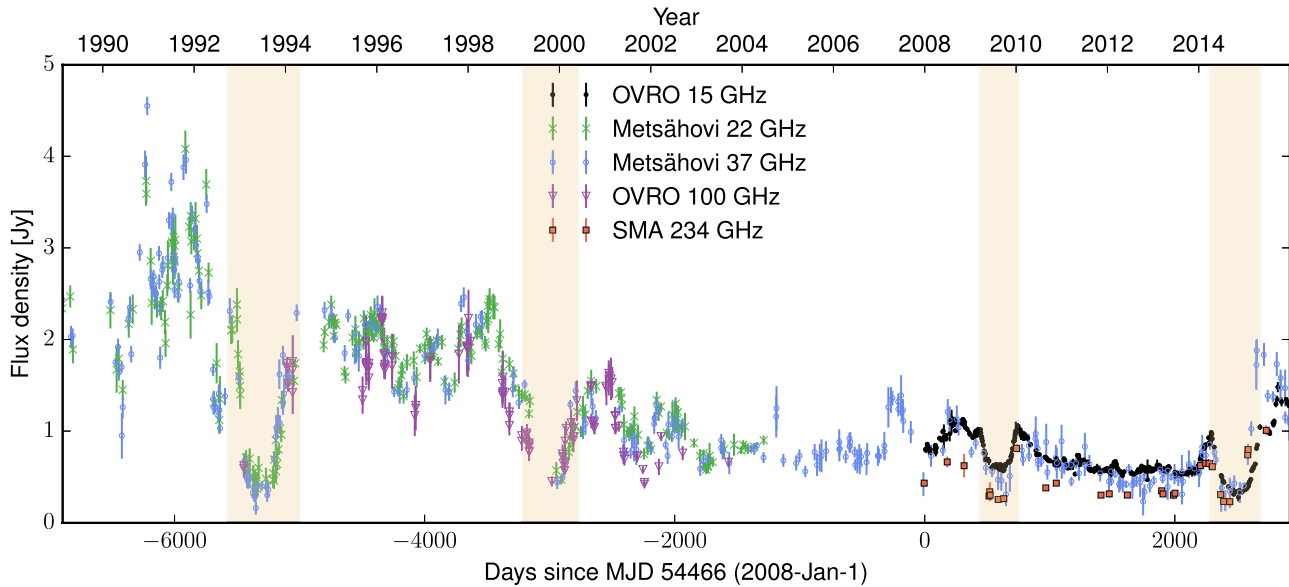
[11] http://tevcat.uchicago.edu/

Figure 2. Same as Figure 1 but with the entire Metsähovi monitoring data at 22 and 37 GHz since 1989, and the OVRO MMA data at 100 GHz. Two more achromatic U-shaped events are seen in 1993 and 2000.

in the error bars. Further details of the reduction and calibration procedures may be found in Richards et al. (2011).

2.2. Metsähovi 22 and 37 GHz

The 22 and 37 GHz observations were made with the 13.7 m diameter Aalto University Metsähovi radio telescope, which is a radome-enclosed Cassegrain antenna in Finland (60°.218 N, 24°.393 E). The measurements were made with 1 GHz-band dual-beam receivers centered at 22.2 and 36.8 GHz, respectively. The high electron mobility transistor front end operates at room temperature. The observations are Dicke-switched ON–ON observations, alternating the source and an adjacent patch of sky in each feed horn. The typical integration time for one flux-density measurement is 1200–1600 s. The detection limit is about 0.2 Jy under optimal conditions. Data points with a signal-to-noise ratio <4 are considered non-detections. The flux-density scale is set by observations of the H II region DR 21. Sources NGC 7027, 3C 274, and 3C 84 are used as secondary calibrators. A detailed description of the data reduction and analysis is given in Teraesranta et al. (1998). The error estimate in the flux density includes the contribution from the measurement rms and the uncertainty of the absolute calibration.

2.3. OVRO 100 GHz

Flux densities in the 3 mm band (100 GHz) were obtained in the period 1992–2003 from the flux density history catalog of the OVRO Millimeter Array (MMA), a six-element millimeter-wave radio telescope array located at the main OVRO site until 2005. The observations were primarily made during dedicated calibration sessions to track the flux density of millimeter-loud blazars and other point sources. The flux-density scale was calibrated using contemporaneous measurements of Uranus and/or Neptune.

2.4. SMA 234 GHz

Flux densities were measured at the Submillimeter Array (SMA), an 8-element interferometer located near the summit of

Maunakea (Hawaii). The measurements were made at frequencies ranging from 221 to 297 GHz; we use the mean frequency of 234 GHz in our analysis. J1415+1320 is included in an ongoing monitoring program at the SMA to determine the flux densities of compact extragalactic radio sources that can be used as calibrators at millimeter and submillimeter wavelengths (Gurwell et al. 2007). Potential calibrators are from time to time observed for 3–5 minutes, and calibrated against known standards, typically solar system objects (Titan, Uranus, Neptune, or Callisto). Data from this program are updated regularly and are available at the SMA website.[12]

3. Symmetric Achromatic Variability (SAV)

In 2009, we observed a roughly 1-year-long highly symmetric U-shaped feature in the OVRO light curve of J1415+1320 and a similar feature was seen in 2014. Figure 1 shows the 15 GHz (OVRO), 37 GHz (Metsähovi), and 234 GHz (SAO) light curves. The U-shaped features are highly achromatic from 15 to 234 GHz, although there are small deviations from perfect achromaticity. We therefore refer to this type of variability as "SAV." The object has also been monitored at 22 and 37 GHz at Metsähovi since 1989, and two more U-shaped features were observed in 1993 and 2000, which were also observed on the OVRO MMA at 100 GHz (Figure 2). Thus, these two additional U-shaped features are also achromatic over the whole observed range—here from 22 to 100 GHz.

The details of the profile of the U-shaped features are seen most clearly in the high-cadence, high-sensitivity OVRO observations from 2008 to 2016 (Figure 1). These show a distinctive mirror symmetry composed of a pair of spikes with time-reversed profiles. As described in Section 5 in the context of gravitational lensing, we can distinguish two types of U-shaped events: a "volcano" type in which the first spike displays a slow rise and a fast decline and the second spike shows a fast rise and slow decline (SRFD–FRSD); and a "crater" type in which a fast rise, slow decline is followed by a

---

3

slow rise, fast decline (FRSD–SRFD). All four events seen in J1415+1320 are of the volcano-type. We see from Figures 1 and 2 that an eight-year period of low intrinsic activity has enabled us to detect SAV clearly in J1415+1320 between 2008 and 2016.

3.1. Incidence of U-shaped Events

Many sources in the complete sample often show "flares" that can have either SRFD or FRSD shape (Hovatta et al. 2008). To test if the observed U-shaped events are due to a chance juxtaposition of two flares, we manually examined our complete sample to derive an approximate estimate for the incidence of U-shaped events of both crater and volcano-type. 981 objects in our sample had light curves of sufficient quality to identify U-shaped events. Among these, we identified 10 U-shaped events in 7 objects (see Figure 9). The probability of a U-shaped feature in 1 of our 981 8 year light curves is therefore $\sim 1\%$. Even among this small sample, J1415+1320 stands out in view of the clarity and isolation of the two U-shaped features relative to the rest of the light curves.

If such U-shaped features are distributed randomly among all the objects, the probability of three or more occurrences in one object in 27 years (J1415+1320) is $\sim 4 \times 10^{-3}$. Though our manual selection criterion is admittedly crude, the extremely low probability suggests that the repeating U-shaped features in J1415+1320 are not random events but are an unusual intrinsic feature of the source itself, due to propagation effects along the lines of sight, or that are a combination of both. Besides this statistical argument, J1415+320 has other unusual properties that have previously led to suggestions that it is being lensed. We explore them in Section 4 below.

4. Radio and Optical Properties of J1415+1320

J1415+1320 has a two-sided jet and exhibits up to eight mas-scale components extending over ~ 60 mas, some of which move outward with speeds ranging from 0.06 to 0.3 mas yr^{-1} and apparent transverse speeds up to $1.5c$ (Kellermann et al. 1998; Perlman et al. 2002; Gugliucci et al. 2005; Lister et al. 2009, 2016). Based on its radio morphology, J1415+1320 is classified as a compact symmetric object (CSO), with radio lobes straddling a bright core (Conway et al. 1992; Wilkinson et al. 1994; Readhead et al. 1996). Although the cores in CSOs are bright (Conway et al. 1992) and variable, the core of J1415+1320 is exceptional—with a core fraction >0.5 (Lister et al. 2009) it is both far brighter and far more variable than most CSO cores in radio galaxies, which have core fractions in the range ~ 0.004–0.06 (Taylor et al. 1996). In addition, J1415+1320 is identified with a spiral galaxy at $z = 0.247$ viewed edge-on (Beichman et al. 1981; McHardy et al. 1991; Carilli et al. 1992), whereas BL-Lac objects are rarely, if ever, hosted by spiral galaxies. The radio core is offset from the optical center of the spiral galaxy by 0.013 arcsec (50 pc) (Perlman et al. 2002). These unusual properties, among others, have led to suggestions that the radio source is an unrelated background object that is being lensed by matter in the spiral galaxy (Carilli et al. 1992; Stocke et al. 1992). We note that based on the number densities of radio sources and intervening galaxies, the probability of such a chance alignment is small (≈ 0.006; details of calculation in Appendix D). However, this probability is based on a posteriori statistics and as such the background source hypothesis cannot be ruled out. If the radio

source is a background object, then due to the lack of multiple images on arcsecond scales (due to lensing by the bulge of the spiral), the redshift of the radio source is bounded by $z \lesssim 0.5$ (Lamer et al. 1999).

4.1. Optical Spectrum of J1415+1320

We obtained an optical spectrum of the spiral galaxy with the low-resolution imaging spectrometer (LRIS; Oke et al. 1995) on the Keck telescope. The data were obtained on MJD 57488.43 with a total exposure time of about 1 hour. The lpipe[13] software was used for bias subtraction, flat-fielding, cosmic-ray rejection, and sky-line subtraction. We then obtained a wavelength solution using arc-lamps and sky lines, optimally extracted the spectrum, and calibrated the flux-density and atmospheric opacity. The resulting spectrum is shown in Figure 3. We detected several emission and absorption lines with high significance, all of which can be attributed to the spiral galaxy at a redshift consistent with that obtained from 21 cm absorption (Carilli et al. 1992). The spectrum also contains some lines (not annotated in Figure 3) detected at low significance that are consistent with $z = 0$ and likely caused by Galactic absorption. We find no clear evidence for an intervening galaxy. We also did not detect broad lines from the AGN, owing to severe extinction by foreground dust-lanes in the spiral galaxy. As such, the redshift of the AGN could not be independently determined.

5. SAVs from Gravitational Lensing

As shown in Section 3, the statistics of occurrence of symmetric U-shaped events makes them unlikely to be caused by random intrinsic fluctuations. In a companion paper (Vedantham et al. 2017), we have studied in detail the possibility that SAV could be caused by ESEs and shown that this explanation for the SAV phenomenon can be ruled out. In this section, we show that the SAVs we observe in J1415 +1320 can be explained naturally and economically by gravitational lensing.

Gravitational lensing is frequency-independent and accounts for the achromatic nature of SAVs. Relatively simple lens configurations yield symmetric magnification patterns. Time-dependent magnification occurs as a source moves over a magnification pattern cast by a foreground lens mass. The most prominent magnification features expected from gravitational lensing are fold caustics (Blandford & Narayan 1986, 1992; Blandford & Kovner 1988). Fold caustics are curves in the source plane where the point source magnification diverges.[14] Rapid brightness changes ensue as a source crosses a fold caustic, and U-shaped features are a result of a closely spaced pair of fold crossings. Such U-shaped events, due to their symmetry, are a telltale sign of lensing, and a powerful discriminant between intrinsic and lensing-induced variability (Schneider et al. 1992).

The generic magnification pattern in gravitational lensing comprises fold curves meeting at cusp points. When a source crosses into a closed fold contour at time t_c, the flux variation shows a rapid rise with a relatively slow decay that follows a $|t - t_c|^{-1/2}$ law (Schneider et al. 1992). This yields an FRSD feature. Source motion in the opposite direction naturally yields

---

[13] http://www.astro.caltech.edu/~dperley/programs/lpipe.html
[14] If we allow the distance of the source to vary, they should be seen as surfaces.
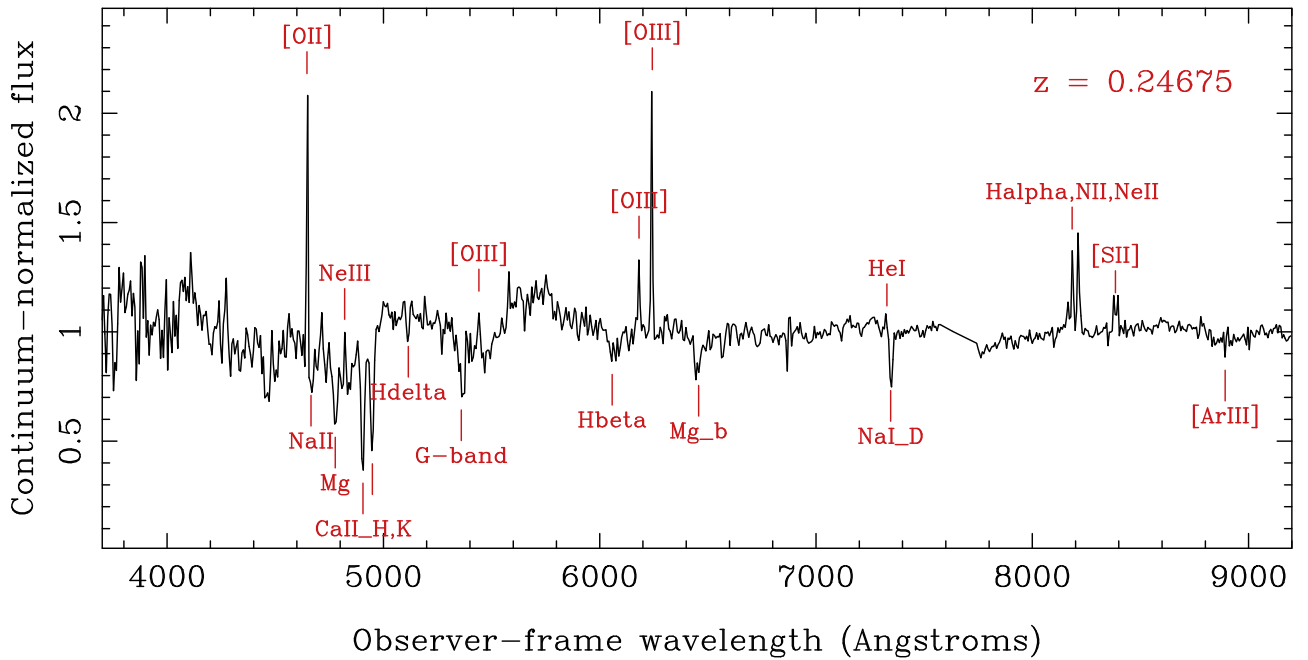
Figure 3. Continuum normalized LRIS spectrum of the putative host of J1415+1320. Prominent lines are marked for a redshift of $z = 0.24675$, which agrees with that determined from H I 21 cm absorption. There is no evidence for emission from an intervening redshift. The artifacts near 6877 and 7613 Å are due to imperfect subtraction of sky lines.

an SRFD curve. Crater symmetries (FRSD–SRFD) occur when a source crosses two folds that meet at a nearby cusp. Volcano symmetries (SRFD–FRSD) occur when a source crosses out of a closed fold contour and subsequently crosses back into it. Successive U-shaped SAV features may or may not come from the same source component; if they come from successive components following a similar track, then we expect the time series to be similar, although the transverse speed may be different, leading to a temporal scaling of the flux density variations.

5.1. An Existence Proof

To establish a "proof of existence" for the gravitational lensing hypothesis, we explored various commonly encountered lens configurations that can yield the basic unit of SAV— a U-shaped event with volcano (SRFD–FRSD) symmetry—as a result of rectilinear motion of the source. Lenses with a high degree of circular symmetry typically yield a four-cusped diamond-shaped caustic configuration (called an astroid). Barring contrived source trajectories, such a lens yields crater-type light curves. The simplest asymmetric lens configuration is a binary lens (the binary need not be gravitationally bound). Binary lenses typically yield a six-cusped caustic pattern that has sufficient complexity to generate a large range of light curve features including both crater and volcano-type SAVs.

We simulated several binary lenses by varying the binary separation d and mass ratio $q < 1$ and found that a range of binary lens parameters can yield the observed U-shaped features for a variety of source trajectories (details of the simulations are presented in Appendix B). We show two examples in Figure 4. The upper two panels (left) show the magnification pattern of a binary lens with a mass ratio of $q = 0.01$ and separation of $d = \theta_E$ (θ_E is the Einstein radius of the more massive object). Since such binary condensates

typically exist in the presence of a smoothly varying background mass distribution (such as in a galaxy), we added a background convergence $\kappa = 0.1$ and shear $\gamma = -0.05$. These values are not very constraining, but are chosen to be "sub-critical, in that the external mass distribution cannot strongly lens the source independently. An approximately south–north source trajectory across the lens (black arrows) generates a single SRFD–FRSD U-shaped event. Hence two compact source components can generate the entire 8-year light curve to good accuracy. Note that we have removed a linear trend from the 15 GHz data points to account for any intrinsic variability of the lensed components or that of unlensed source components away from the caustics.

The bottom panel of Figure 4 shows an alternative binary model that can reproduce both U-shaped features with only one moving radio component rather than two. However, this model requires the source to "graze" the caustic pattern, making the set of plausible source trajectories somewhat restrictive.

The above fits were obtained by manually varying the lens and source parameters. In particular, the crossing timescale, and hence the source speed, are largely set by the relative timing of the four peaks that comprise the two U-shaped events in 2009 and 2014. The source components' sizes and flux densities are largely determined by the peak-magnification at the caustics. These two factors are somewhat degenerate, because the magnification near a fold caustic is expected to follow $\mu = \alpha p^{-1/2}$, where $p = \sigma_s/\theta_E$ where the source is modeled as a Gaussian with standard deviation σ_s, and $\alpha \approx 1$ depends on the precise nature of the Fermat potential at the fold. Hence a weaker smaller source can generate a caustic peak with a similar flux density as a stronger larger source. However, by exploring a large parameter range, we found that the source components must be smaller than $\approx 0.03\,\theta_E$ to account for the precise light curve *profile* around the caustic crossing. For the family of lens models considered here
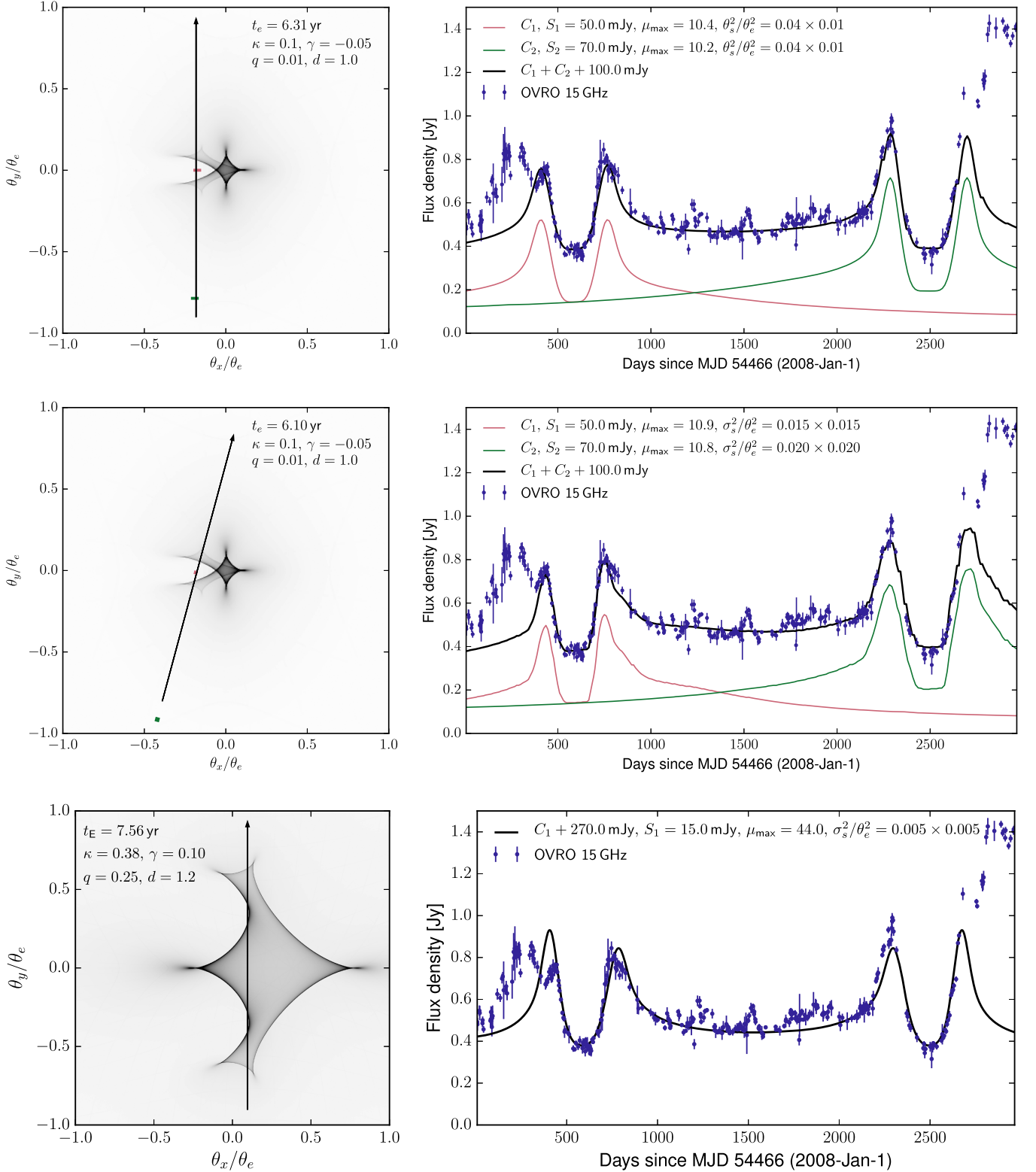
Figure 4. Fits to the OVRO 15 GHz data for two lens models. A linear function of time has been subtracted from the data. The left panels show the magnification pattern, and the right panels show the model light curves. The top two rows have the same lens model but different trajectories for the two source components (red and green). The right panels show the light curves for the individual components (green and red) and their sum (black). The lens model in the bottommost row requires only one source component but the range of plausible trajectories is limited. Lens and source parameter values are shown in the embedded text.

we found $2.5 \lesssim \alpha \lesssim 4.25$. Table 1 summarizes the parameter values for two lens models presented in Figure 4.

A hallmark of gravitational lensing is its achromaticity, although we expect some chromaticity due to variation of

source size and centroid position with frequency. Such variation is expected in the emission from relativistic jets due to a combination of the evolution of the emitting population of relativistic electrons with time and location in the jet, and

Table 1
Summary of Lens and Source Parameters Used in the Model Fits from Figure 4

q	d/θ_e	κ	γ	t_E (years)	θ_E (μas)	$v_\perp/c$	$p = \sigma_s/\theta_E$
0.25	1.2	0.38	0.1	7.54	81	0.33	0.01×0.01
0.01	1.0	0.1	−0.05	6.31	87.3	0.42	0.04×0.01

Note. The columns represent the binary mass ratio q, binary separation d, external convergence κ, external shear γ, Einstein crossing time t_E, Einstein radius θ_E, transverse speed of the source $v_\perp$, and source size p. The Einstein angle assumes a source brightness temperature of $T_b = 10^{13}$ K, and the transverse speed values are based on a nominal source redshift of $z_s = 0.5$ (cosmological time dilation included).

synchrotron opacity effects. To test if the binary lens models from Figure 4 reproduce the 37 and 234 GHz observations, we assumed that (i) the source component size varies with frequency ν as ν^{-1}, (ii) the flux densities of the unlensed source components have a spectral index of $\alpha = -0.7$, and (iii) the lensed components have a flatter spectral index of $\alpha = -0.1$. With these assumptions, we predicted the corresponding light curves at 37 and 234 GHz where data are available. Figure 5 shows the multifrequency data and the expected light curves for the lens model shown in the upper row of Figure 4. Despite simplistic assumptions on the source properties, the fits are quite good over a factor of 15 in wavelength.

The data show small but significant departures from both model light curves, which may be due to intrinsic variability or due to our simplistic assumptions of both the source and lens. For instance, there is evidence for additional symmetries in the light curves (see Appendix C), which may be accounted for by lenses with a larger number of mass condensates that give rise to caustic networks with higher complexity (Schneider & Weiss 1987; Blandford & Kovner 1988). Nevertheless, the models satisfactorily account for the symmetry and profile of the SAV features and serve as an "existence proof" for the gravitational lensing hypothesis.

5.2. Constraints on Lens Properties

Having seen that simple lens models can produce the observed SAV features in J1415+1320, we now place constraints on the physical properties of the putative lens. Although several lens configurations are viable, fold caustics have generic properties that enable us to constrain the lens parameters almost independently of the precise lens configuration.

We constrain the lens mass, M, by placing bounds on the Einstein radius, θ_E, that sets the natural length and angular scale for lensing (Blandford & Narayan 1992):

$$\theta_E = (4GM/c^2D)^{1/2}$$
$$\approx 90(M/10^3 \, M_\odot)^{1/2}(D/1 \text{ Gpc})^{-1/2} \, \mu\text{as}. \quad (1)$$

Here, G is the gravitational constant, and $D = D_l D_s / D_{ls}$, where D_l and D_s are the observer-lens and observer-source distance and D_{ls} is the lens-source distance. All distances are angular-diameter distances. Lensing causes multiple imaging with separations of up to $\approx 2\theta_E$. There is no evidence for multiple imaging in 15 GHz MOJAVE VLBI observations (Lister et al. 2009, 2016) at 23 epochs between 1995 and 2011. The observations had a resolution of about 1 mas. By conservatively assuming that image splitting at 0.5 mas would be detectable, we place an upper bound on the Einstein radius: $\theta_E < 250 \, \mu$as. Jets in AG usually exhibit moving features that

propagate away from the core. If the jet is directed close to our line of sight the apparent speed can be superluminal (Begelman et al. 1984). In AGs at cosmological redshifts this probes lenses with Einstein radii $\sim 100(v_\perp/c)(t/1 \text{ year})\mu$as.

A lower bound on θ_E can be placed using constraints on the sizes of synchrotron sources. For lensing to yield considerable magnification, the source must be significantly smaller than θ_E. Fits to the precise profile of the observed SAV require

$$p = \sigma_s/\theta_E \lesssim 0.03. \quad (2)$$

However, radio sources of a given flux density cannot have a size smaller than a threshold below which inverse Compton losses rapidly "cool" the relativistic plasma. This sets an upper limit of $\sim 10^{12}$ K on the intrinsic brightness of an incoherent synchrotron source, though brightness temperatures of $T_b \gtrsim 10^{13}$ K have been observed in compact components in AG jets (Johnson et al. 2016), likely caused by relativistic Doppler boosting. If the source has a Gaussian brightness profile, the brightness temperature can be related to the observed source flux density by the Rayleigh−Jeans law:

$$S_0 = \mu \frac{2kT_b\lambda^2}{2}\pi\sigma_s^2, \quad (3)$$

where k is Boltzmann's constant, λ is the wavelength, and μ is the lensing magnification. Since the Fermat potential near fold caustics has a generic functional form, the peak magnification near a fold also has a generic form (Schneider & Weiss 1992):

$$\mu_{\text{max}} \approx 2.5 p^{-1/2}, \quad (4)$$

where the constant of proportionality has been determined numerically (see Appendix B). Equations (1)–(4) can then be used to put a lower limit on the Einstein radius:

$$\theta_E^2 \geqslant \frac{S_o\lambda^2}{2.5p^{1.5}4\pi kT_b}. \quad (5)$$

The mass of the lens can then be determined from θ_E for any given lensing geometry.

In the case of J1415+1320, the peak-to-trough flux-density change for the U-shaped events is $S_o \approx 0.5$ Jy at 15 GHz and we assume $p = 0.03$. Figure 6 shows the lower bounds of the lens mass and Einstein radius for geometries where the radio source is located in the spiral and where it is a background radio source. Since the intrinsic sizes of the lensed source components are not precisely known, we plot the constraints corresponding to values of T_b in the range of 10^{12}–10^{14} K.

5.3. The Location and Mass of the Lens

Due to the ambiguity in the location of the radio source (see Section 4), we discuss both possibilities: (i) the radio source is
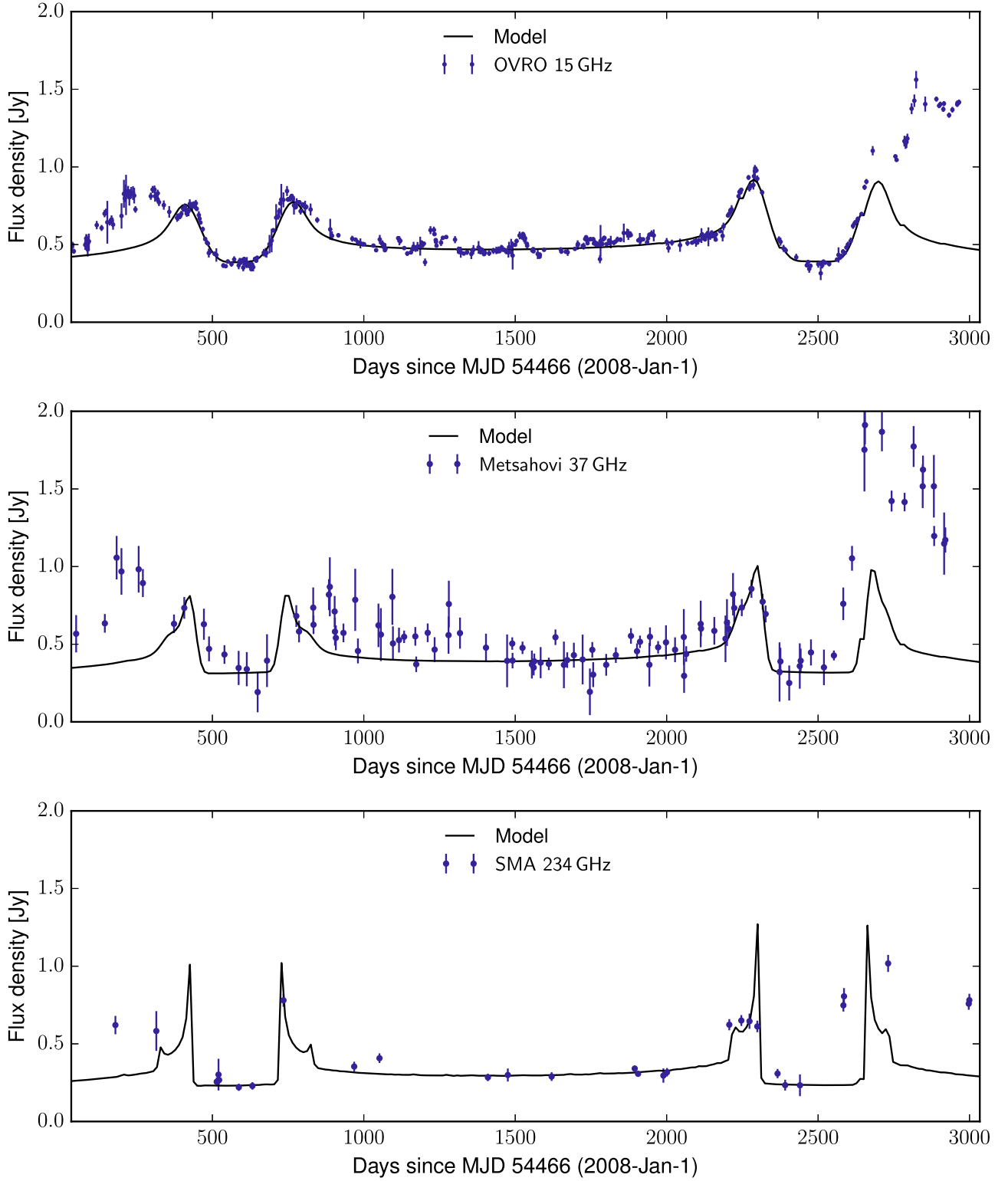
Figure 5. Multifrequency model light curves overplotted on data at 15, 37, and 234 GHz. The lens model and source trajectories are the same as that in the topmost row of Figure 4.

located in the $z = 0.247$ spiral, and (ii) the radio source is an unrelated background object. In the former configuration, we can rule out all models in which the lens lies in our Galaxy; Galactic lenses consistent with the light curves of J1415+1320 have a mass range consistent with optical microlensing surveys. Such surveys (Alcock et al. 2000) find lensing probabilities of about 10^{-7}, and crossing times of several days,

whereas we have found a crossing timescale of ≈ 1 year. If both the source and the lens are in the spiral galaxy, the lens would need to be a $\gtrsim 10^6 \, M_\odot$ black hole. Since we do not find such objects in the spiral arms in our own Galaxy, we discount this possibility. The remaining possibility is that the lens lies between our Galaxy and the spiral host of the radio source. Here the requirements on the lens mass and projected density
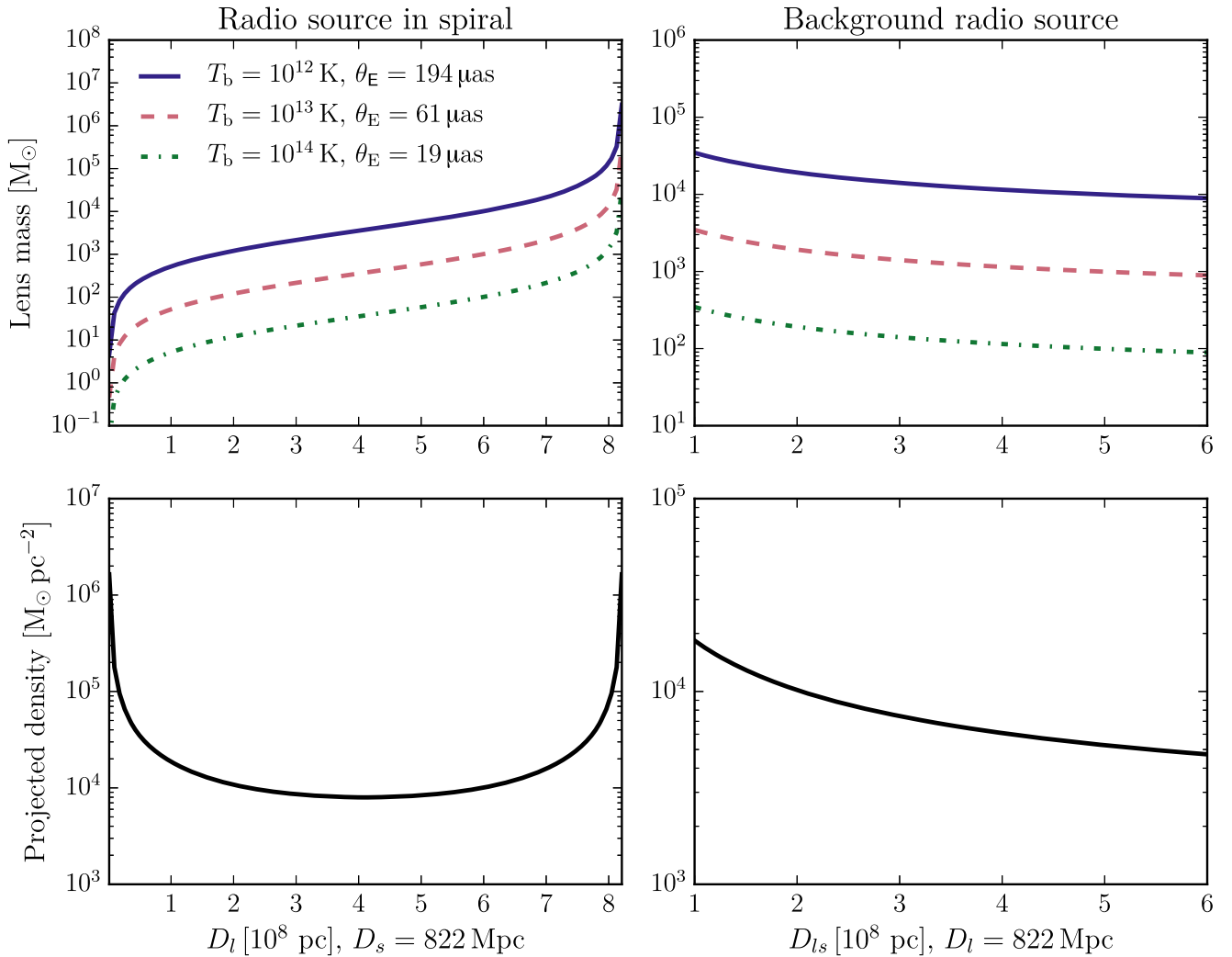
Figure 6. Constraints on the minimum lens mass (top panels), and projected mass density (bottom panels). The left and right columns correspond to geometries where the radio source is in the putative spiral host, and where the radio source is an unrelated background object, respectively. The curves are plotted as a function of observer-lens distance, D_l, and the source-lens distance, D_{ls}, for the two geometries.

are $\gtrsim 10^3 \, M_\odot$ and $\gtrsim 10^4 \, M_\odot \, \mathrm{pc}^{-2}$. As discussed in Section 4.1, we obtained a deep optical spectrum of J1415+1320 with the Keck telescope and we did not find evidence of an intervening galaxy, although a faint dwarf galaxy could have evaded detection. In the scenario where the radio source is located in the spiral galaxy at $z = 0.247$ there are thus three awkward facts that must be accepted: (i) J1415+1320 is unique in being a BL Lac object and a CSO located in a spiral rather than in an elliptical galaxy, (ii) there is a 50 pc offset between the radio source and the optical nucleus, and (iii) the lens is an invisible intergalactic object, possibly a dwarf elliptical galaxy.

In the alternative hypothesis the radio source is a background object and the foreground spiral galaxy provides a natural host for the lens. The absence of multiple imaging on arcsecond scales due to lensing by the spiral's bulge limits the redshift of the radio source to be $z \lesssim 0.5$ (Lamer et al. 1999). In addition, the angular size of interstellar scattering (ISS) in the spiral must be significantly smaller than the Einstein radius for ISS not to "quench" the lensing signatures. Non-detection of ISS at a wavelength of 18 cm (Perlman et al. 1996) shows that any scattering of the J1415+1320 emission by the spiral is low compared to several nuclear sightlines through our own Galaxy at low latitudes. However, ISS in our Galaxy is patchy, and

little is known about ISS in other galaxies. In the background source scenario, there are two awkward facts that must be accepted: (i) the low probability of such an alignment, and (ii) the anomalously low ISS, but (i) is an a posteriori argument and (ii) is based on assumptions regarding ISS that cannot be substantiated by current observations. For these reasons, the background source argument is preferred, though not compelling. In any case, we see from Figure 6 that the similar constraints on the lens mass ($\gtrsim 10^3 \, M_\odot$) and projected density ($\gtrsim 10^4 \, M_\odot \, \mathrm{pc}^{-2}$) apply to this geometry too.

6. Discussion

In this section, we consider the implications of the results obtained thus far and make falsifiable predictions to further test the hypothesis that gravitational lensing is the cause of SAV.

6.1. Cosmological Density of Intermediate-mass Lenses

The incidence of lensing may be used to constrain the cosmological fraction of matter in the putative lenses (Press & Gunn 1973). We adopt the *Planck* cosmological parameters: $H_0 = 67.8 \, \mathrm{km \, s^{-1} \, Mpc^{-1}}$, $\Omega_m = 0.308$, $\Omega_\Lambda = 1 - \Omega_m$, $\Omega_k = 0$. Assuming a flat universe, this yields a critical density of
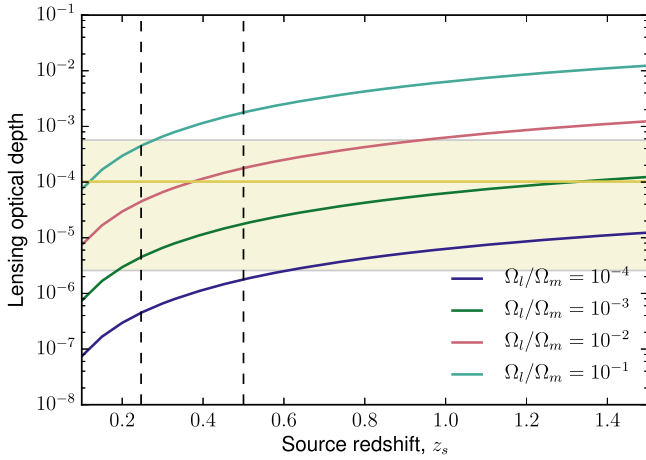
Figure 7. Fraction of lines of sight intercepted by the putative lens population (lensing optical depth) as a function of source redshift. The curves correspond to cases where different fractions of the cosmological matter density are in the lenses. The horizontal yellow line corresponds to the observed probability of intercepting a lens (based on just one sample, J1415+1320), and the shaded region is the corresponding 95% confidence interval assuming Poisson statistics.

$\rho_c = 3H_0^2/(8\pi G) = 8.633 \times 10^{-27}\,\mathrm{kg\,m^{-3}}$. Let a fraction f of the matter be in the putative lenses of mass M. The comoving number density of lenses is then $n = f\Omega_m \rho_c/M$. Consider a comoving volume element at redshift z_l of $dV(z_l) = (c/H_0)(1 + z_l)^2 D_l^2/E(z_l)d\Omega dz_l$, where $E(z) = \sqrt{(1 + z)^3 \Omega_m + \Omega_\Lambda}$. There are, on average, ndV lenses in this volume element. Each lens presents a strong-lensing cross-section of $\pi\theta_e^2$. The fractional sky area occupied by all lenses out to the source redshift is therefore

$$\tau(z_s) = \frac{1}{4\pi}\int ndV(z_l)\pi\theta_e^2. \tag{6}$$

Substituting for n, dV, and θ_e, we get

$$\tau(z_s) = \left(\frac{c}{H_0}\right)\int_{z=0}^{z=z_s} dz\,\frac{Gf\Omega_m}{c^2}\frac{D_{ls}}{D_l D_s}$$
$$\times \frac{(1 + z)^2}{\sqrt{(1 + z)^3 \Omega_m + \Omega_\Lambda}} \tag{7}$$

Figure 7 shows the expected lensing optical depth for various values of matter densities in the putative lenses $\Omega_l = f\Omega_m$, as a function of source redshift. To estimate Ω_l, these curves must be compared to the *observed* probability of lensing—one lensed source among a sample of 981 objects, assuming J1415+1320 is unique in the sample. Because lensed objects have larger apparent brightness, they are overrepresented in any flux density-limited samples such as the CGRaBS sample. This magnification bias factor largely depends on the faint-end luminosity distribution of the specific source population under consideration, and the properties of the lens population. Both of these are difficult to establish, especially given our postulate of a new population of intermediate-mass lenses. We adopt a bias factor of 10 to derive an order-of-magnitude estimate. Accounting for this magnification bias, we find that one in 981 × 10 sightlines must be intercepted by the putative lenses. The errors on this lensing rate are large with just one sample, but they can be quantified by assuming Poisson statistics for the incidence of lensing. In Figure 7 we show the 95% confidence bounds on the lensing rate parameter

as a yellow box. Figure 7 shows that for a source redshift of $z_s = 0.5$, a 95% bound of $10^{-4}\Omega_m$ to $3 \times 10^{-2}\Omega_m$ may be placed on the comoving density of the putative intermediate-mass lenses. Hence, if the lensing hypothesis is shown to be true, then a non-trivial fraction of the cosmological matter density must exist in intermediate-mass objects with projected densities of $\gtrsim 10^4\,M_\odot\,\mathrm{pc^{-2}}$.

6.2. Falsifiable Predictions

Our hypothesis that links SAVs to gravitational milli-lensing leads to several key predictions:

(i) Intensive high-cadence long-term monitoring of J1415 +1320 at multiple frequencies should detect further SAV events as new compact source components traverse the lens.

(ii) The incidence of SAVs should increase with redshift (see Figure 8).

(iii) During future SAV events, global millimeter-wave VLBI observations should be able to detect creation and annihilation of lensing images on ∼1 year timescales (see also Gopal-Krishna & Subramanian 1996). The lensed images form at a typical separation of $\approx 2\theta_E \gtrsim 100\,\mu$as which can be resolved by existing VLBI facilities. Bright image pairs will be closer than $2\theta_E$, however they will brighten and merge, or fade and separate in a manner that will be accessible to multi-epoch millimeter VLBI.

(iv) The polarization position angle of the multiply lensed images should not change around caustic crossings.

(v) Finally, if the recently discovered fast radio bursts (Lorimer et al. 2007) are at cosmological distances, then they must also be milli-lensed at a rate comparable to AG (Muñoz et al. 2016). In such cases, $\lesssim 10$ ms time delays between lensed images of the burst might be detectable with upcoming surveys.

6.3. SAV in the BL Lac Object AO 0235+164

The prominence of the two SAV events in J1415+1320 in 2009 and 2014 suggests the possibility that such signatures of radio milli-lensing may have been seen in other objects. For instance SAV may have been seen before, in the BL Lac object AO 0235+164. In the University of Michigan Radio Astronomy Observatory low-frequency light curves of Aller et al. (2003, Figure 1), as well as the 22–90 GHz light curves of Nieppola et al. (2009, Figure 2), there is a symmetric crater U-shaped feature between 1994 and 1999, and the variability was achromatic from radio to optical frequencies (Webb et al. 2000), although no optical observations are available for the first half of the crater feature.

In Figure 8 we show the Metsähovi 22 and 37 GHz light curves and the R and B band light curves (Webb et al. 2000) at high time resolution. Here the overall symmetry between 1994 and 1999 is again clear, although there are also some departures from symmetry, such as might be caused by intrinsic variability in the radio source flux density and speed, and by the presence of multiple lensed components. The highly correlated variations from radio to optical frequencies over the whole time interval could be produced by one radio component or several, moving behind a caustic network. Gravitational lensing has been invoked to explain various optical emission features of
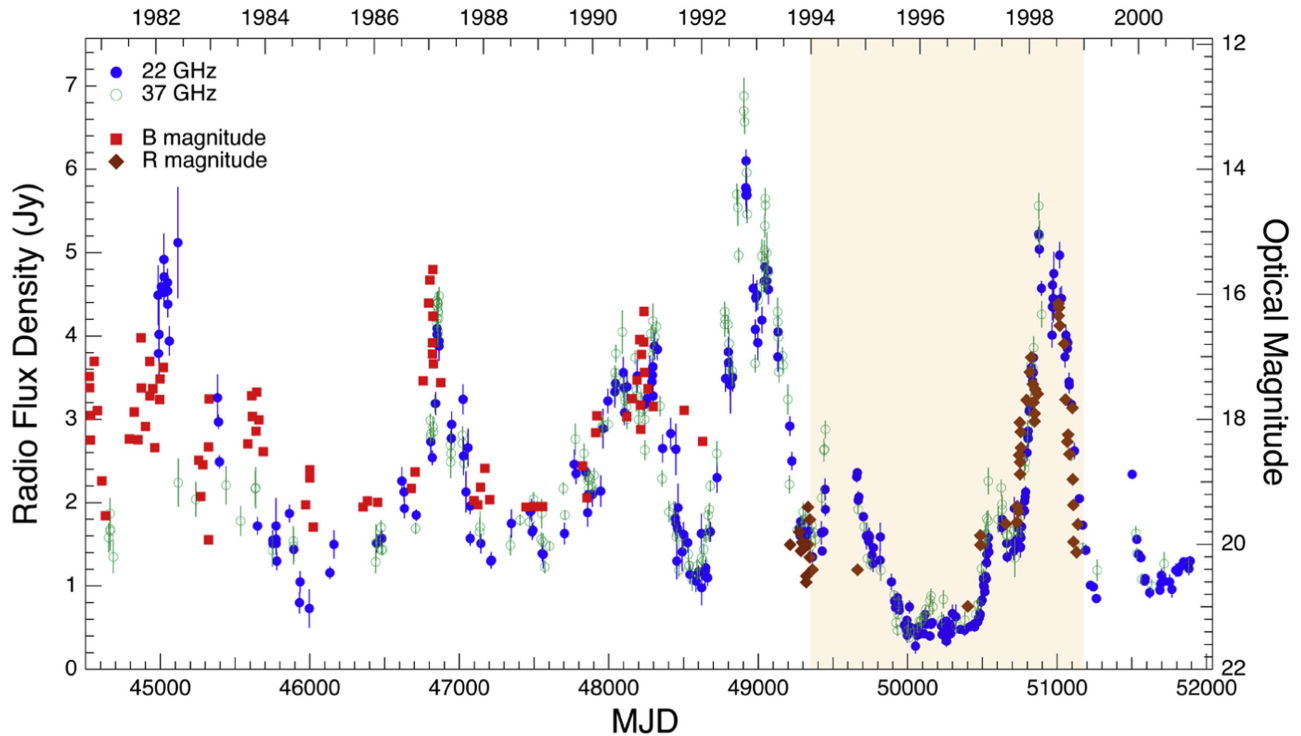
Figure 8. The variability in AO 0235+164 at 22 and 37 GHz and *B* and *R* magnitudes (Webb et al. 2000; Nieppola et al. 2009). The roughly 5-year-long putative SAV is highlighted.

AO 0235+164 (Stickel et al. 1988; Webb et al. 2000). The object has a redshift $z = 0.940$ with intervening absorption systems at $z = 0.852$ and 0.524 (Cohen et al. 1987), each of which could have one or several lenses associated with it. Detection of image splitting with high-resolution ($\lesssim 100\ \mu$as) global millimeter-wave VLBI observations is one avenue to ascertaining the presence or absence of milli-lensing in such SAV candidate sources.

It is worth emphasizing here that the two objects in which we find the clearest evidence of SAV, J1415+1320 and AO 0235 +164, have both long been suspected of being subject to gravitational lensing (Stickel et al. 1988; Carilli et al. 1992; Stocke et al. 1992; Webb et al. 2000), and that our monitoring observations have led us, via the completely new and previously unsuspected phenomenon of SAV, to this same hypothesis.

6.4. Outlook

We have presented a rare new form of variability in AG that is time-symmetric and achromatic in nature. We propose that such variations are a result of gravitational lensing, wherein compact source components cross the magnification pattern of a gravitational lens at relativistic speeds. SAV may therefore provide a powerful new tool for investigating not only the cores of AG but also the putative lenses. These lenses have masses in the range 10^3–$10^6 M_\odot$—a range that embraces intermediate-mass black holes, cores of globular clusters, dense molecular cloud cores, and compact dark matter halos (Carr 1994). The incidence of SAV in our sample suggests that a non-trivial fraction of the cosmological mass may be in such lenses, though meaningful constraints cannot be placed with just one or two examples.

If SAV is confirmed to be due to gravitational milli-lensing it resolves the longstanding puzzles (Stickel et al. 1988; Carilli

et al. 1992; Stocke et al. 1992) over the high brightness and strong variability of the cores of J1415+1320 and AO 0235 +164, as well as the absence of a narrow emission-line region and the low thermal IR flux of J1415+1320. It would confirm the hypothesis posed some decades ago that a subset of variability in AG is due to gravitational lensing (Subramanian et al. 1985; Schneider & Weiss 1987; Gopal-Krishna & Subramanian 1991). In addition, it will bolster theories that posit that some members of the parent BL Lac population are inherently fainter and less variable (Ostriker & Vietri 1985, 1990), although these papers were suggesting permanent magnification and not what we are seeing in SAVs.

In the 2014 SAV in J1415+1320 it appears that the millimeter radiation leads the centimeter radiation (Figure 1). This is not seen in the 2009 SAV, but there the millimeter sampling is sparse. Similarly, in AO 0235+164 there are some hints that the optical variations may precede the radio variations (see Figure 8). If our gravitational lensing hypothesis for SAV behavior is confirmed, and furthermore if these objects are not anomalous, they could have profound implications for our interpretation of the relationship between the high-frequency and the low-frequency emission regions observed in AG jets. This behavior is readily interpretable if the moving features are outwardly propagating particle acceleration/ magnetic amplification fronts—shocks if the jet is plasma-dominated and nonlinear hydromagnetic waves if electromagnetic field is dominant. The optically emitting electrons would cool close to the front and the centroid of their emission would cross any caustic ahead of the radio emission. Early shock-in-jet models (Marscher & Gear 1985) showed that millimeter variations lead centimeter variations in AG and would seem to fit this model. The alternative interpretation of multifrequency observations of AG jets is that the higher-frequency emission originates further back along the jet toward

the core, rather than further out along the jet away from the core, since it is well-known from VLBI observations that this is often the case at centimeter wavelengths in AG (Readhead et al. 1978; Readhead 1980). Whether this is the case in all AG and over a much wider frequency range is by no means clear. The additional resolution that SAV may provide under the lensing hypothesis could well then be the only direct way of exploring this interesting dichotomy other than via submilli-meter VLBI from space.

The failure to associate dark matter with an elementary particle has revitalized interest in the idea that there may be a large population of primordial black holes (Carr et al. 2016). Further monitoring of relativistically moving radio source components in large samples of radio sources, combined with millimeter-wave VLBI imaging at $\lesssim 100\,\mu$as scales may provide a new and sensitive approach to constrain this putative population.

We end by noting that it is the time-symmetry and achromaticity of SAV that motivated the gravitational lensing hypothesis. If this hypothesis is falsified, then it would imply that SAV is intrinsic to the source, and pose an intriguing challenge to our understanding of relativistic jets. Attempts to reproduce intrinsic SAV features may provide critical insights into the emission geometry and mechanism in such jets.

Appendix A
False Alarm Probability

Lensing yields time-symmetric and achromatic light curves but they need not have the characteristic U-shape seen in J1415 +1320. Here we have searched for U-shaped profiles in the OVRO data not necessarily to find milli-lensing candidates, but as a means to conduct a blind test of the null hypothesis: the SAVs in J1415+1320 are caused by stochastic fluctuations, where the "arrival" of U-shaped events is a Poisson process. Because the precise profile of the U-shaped events is not known a priori, automated searching for such events in our sample is non-trivial, and previous automated attempts (searches for ESEs) have only attained limited success (see for e.g., Lazio et al. 2001). We have embarked on an effort to develop algorithms for automated detection of SAVs, but here we employ human inspection (independently done by two co-authors) of the OVRO light curve to get an "order-of-magnitude" estimate of the false alarm rate. Figure 9 shows

the U-shaped events thus identified in the OVRO database. We note that, it is the repeating nature of U-shaped events in J1415 +1320 that yield an extremely low false alarm-rate as computed in Section 3. Multiple U-shaped events are also seen in J0310+3814, but this object also shows a significantly larger amount of non-SAV variability than J1415+1320, and more importantly, it is unknown if the events in J0310+3814 are achromatic. We also note that if shown to be chromatic, the U-shaped events in Figure 9 will be candidate ESEs (Fiedler et al. 1987).

Appendix B
Lens Modeling

B.1. Rayshooting Simulation

We employ the usual dimensionless units where all angles are expressed in units of the Einstein radius, $\theta_{\rm E}$. Let the source and lens plane angular coordinates (two-dimensional) be $\boldsymbol{y} = [y_1, y_2]$ and $\boldsymbol{x} = [x_1, x_2]$, respectively. The lens equation relates the image-plane and source plane coordinates of light rays traveling from the source to the observer. For the single point-mass case, the lens equation is Schneider et al. (1992, chap. 8.1.2):

$$\boldsymbol{y} = \boldsymbol{x} - \frac{\boldsymbol{x}}{|\boldsymbol{x}|^2}, \qquad (8)$$

where the second term on the right side is the gradient of the Fermat potential and is the angle by which the light rays are deflected by the lens. Consider a binary mass comprising two point-like objects of mass 1 and q located, respectively, at $0 = [0, 0]$ and $\boldsymbol{d} = [d, 0]$. The lens equation then needs to include the contributions of both masses.

The influence of an external smooth mass distribution can be parameterized by the convergence κ and shear γ. The shear in particular accounts for any ellipticity in the external mass distribution.

The total deflection is then (Schneider et al. 1992, chap. 8.2.2):

$$\boldsymbol{y} = \boldsymbol{x} - \frac{\boldsymbol{x}}{|\boldsymbol{x}|^2} - q\,\frac{\boldsymbol{x} - \boldsymbol{d}}{|\boldsymbol{x} - \boldsymbol{d}|^2} - \begin{pmatrix} \kappa + \gamma & 0 \\ 0 & \kappa - \gamma \end{pmatrix} \cdot \boldsymbol{x}, \quad (9)$$

where "·" denotes matrix multiplication. We have chosen the principal axes for the ellipticity of the external mass to lie along the coordinate axes, so the off-diagonal elements in the last term of Equation (9) are zero. A positive γ enhances ray deflection along the x_1 axes as compared to the x_2 axes; this corresponds to an external mass distribution that is stretched along the x_2 axis. Our models therefore make the implicit assumption that the binary axis lies along one of the cardinal axes of the external mass distribution's ellipticity. Relaxing this assumption extends the parameter space considerably and is not necessary to find adequate models.

We used Equation (9) to simulate the magnification patterns using the technique of inverse-ray-shooting. We follow a large number of rays from the observer to the source plane. We "shot" about 10^8 rays on a regular grid on $\boldsymbol{x}$. Using Equation (9), we compute the source plane location $\boldsymbol{y}$ of each ray. The rays are then binned on a suitable source plane grid. Because lensing preserves surface brightness, the magnification is the ratio of the image area to the source area on the sky. The magnification for each source bin is thus the ratio between the
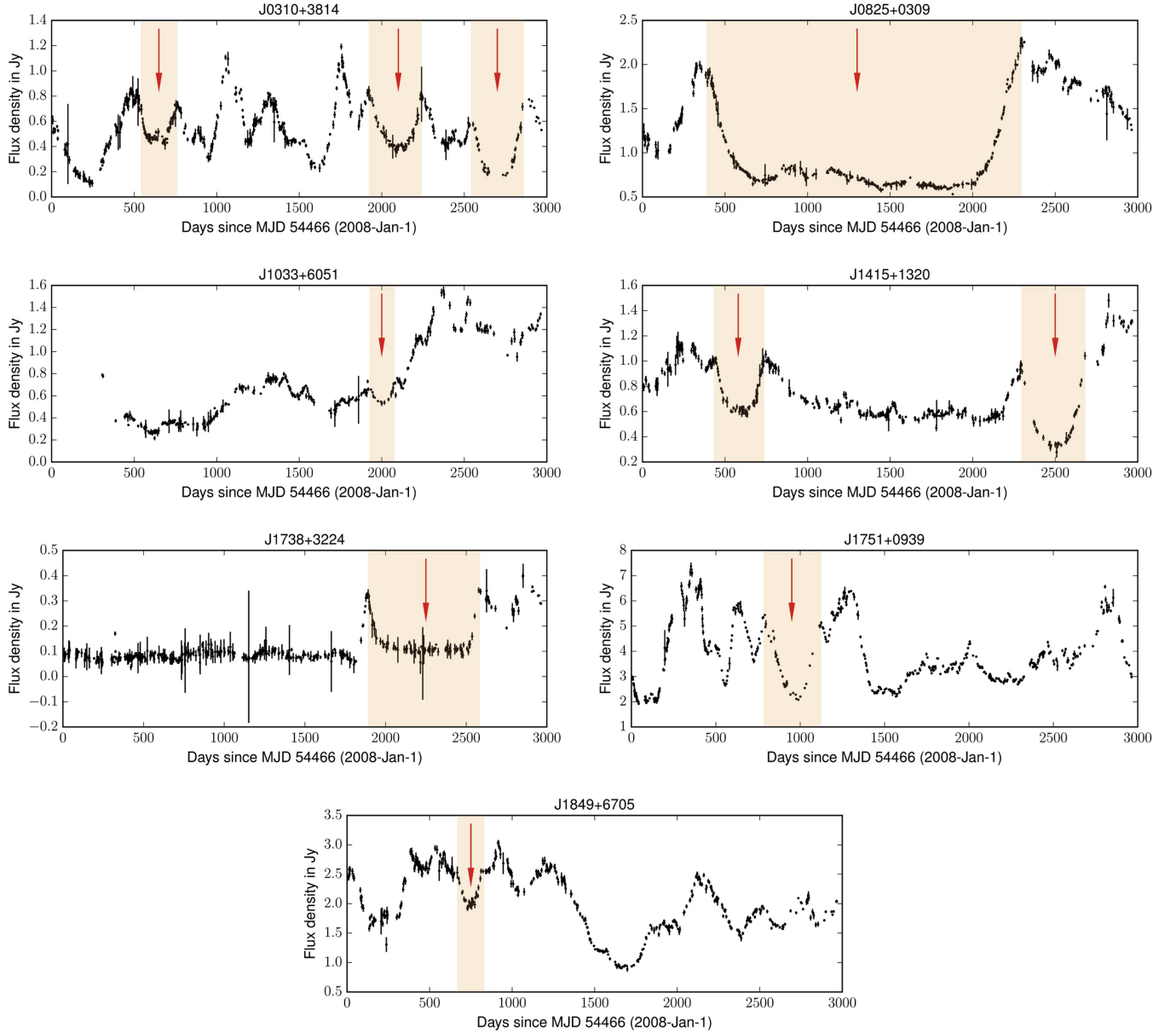
Figure 9. OVRO 15 GHz light curves of seven objects in which U-shaped features were detected. The 10 features are indicated with arrows.

number of rays in the bin and the number of rays in the absence of the lens deflection. The lens models used here are simple enough for the computation to be done on a desktop within reasonable compute-time (<1 minute).

B.2. Rationale for Choice of Lens Configuration

We endeavored to generate a SRFD–FRSD "volcano" type light curve from a lens model that has the following properties: (i) the lenses should resemble commonplace astrophysical objects (point-like masses, elliptical halos, etc.), (ii) the lens model should be economical—simple models are favored; and (iii) a rectilinear source trajectory should yield the required SRFD–FRSD symmetry.

We started with the simplest lens of all—an isolated point-mass lens (axially symmetric gravitational field). Such a lens has a point-like singularity in its source plane magnification pattern, and therefore yields a FRFD light curve, which cannot adequately describe the data. Elliptical perturbations to a point-like lens typically yield a FRSD–SRFD (crater-type) light curve that is also not viable. Next, we considered binary lenses, which can yield a rich phenomenology of light curves for various values of the mass ratio $q \leqslant 1$ and separation d. We computed a library of magnification patterns by varying q and d and identified two scenarios that yield favorable magnification patterns: (i) an asymmetric ($q \ll 1$) binary with $d \sim 1$, and (ii) a binary with comparable masses ($q \lesssim 1$) with wider separation $d \gtrsim 1$. The corresponding magnification patterns are shown in Figure 10, along with example source trajectories that give the SRFD–FRSD volcano-type light curve. For brevity, we will refer to the two lens models as "cupid's bow" and "barbed arrow," respectively.

B.3. External Mass Sheet

Having identified two promising candidate lens configurations, we then perturbed the lens parameters to account for (i) the relative timing of the four caustic crossings that together
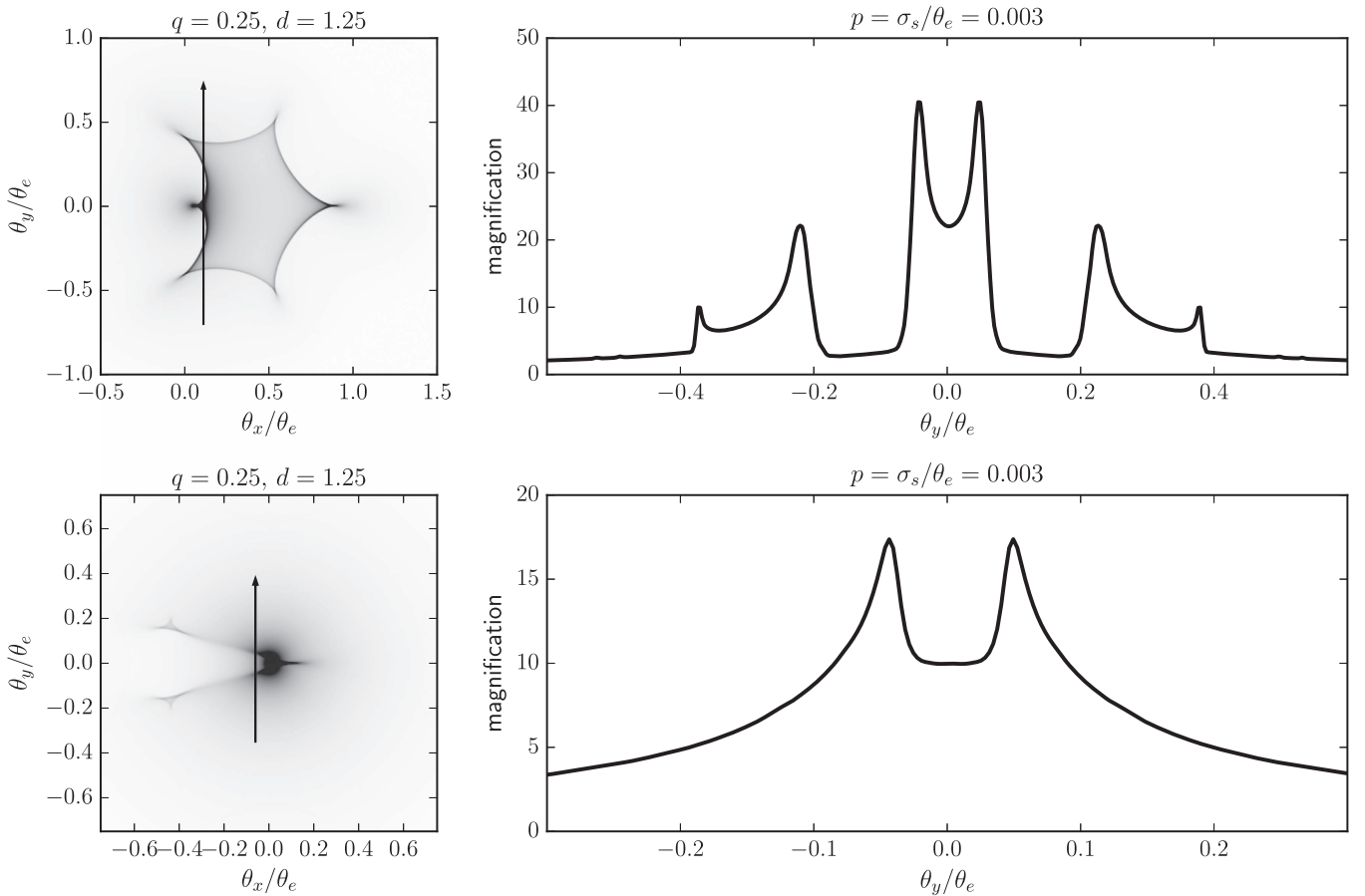
13

Figure 10. Two binary lens configurations (top and bottom rows) that yield the required SRFD−FRSD parity. Top left: magnification pattern for a binary lens with $q = 0.25$, and $d = 1.25$ (the "cupid's bow"). Top right: magnification pattern for a source trajectory given by the black arrow. Bottom left and right: similar to the top panels, but for a lens with $q = 0.01$, and $d = 0.8$ (the "barbed arrow"). The top model can yield the two U-shaped parameters with a single source component, but the viable set of source trajectories is restrictive. The bottom model needs two source components to achieve two U-shaped events but admits a much larger range of source trajectories.

yield the two U-shaped features, and (ii) the flux-density levels throughout the 2008–2016 period. These two constraints can be satisfied by the addition of a smooth background gravitational potential. Such a background potential could reasonably originate in the distributed mass of the galaxy that hosts the lens (Chang & Refsdal 1979).

If $\kappa + |\gamma| > 0.5$, then the background mass has sufficient lensing strength to independently create multiple images on the macro scale (typically, arcseconds). Since no arcsecond-level image splitting has been observed in J1415+1320, we imposed the constraint $\kappa + |\gamma| < 0.5$. We again simulated a library of magnification patterns with this constraint and found that a large range of (κ, γ, q, d) parameter values can "fit" the light curves. The introduction of external mass is therefore required but is not very constraining. Two examples of favorable lens models that are perturbations of the cupid's bow and barbed arrow lenses are presented in Figure 4.

B.4. Model Light Curve Fits to Multifrequency Data

We obtained a model light curve fit to the OVRO 15 GHz data as follows. The data (Figure 1) show a linear decreasing trend in flux density over decade timescales, which may be due to variation in the unlensed source components. We subtracted the linear function of time, $S_{\mathrm{lin}}(t) = -1.397 \times 10^{-4}t + 7.922$, from the data, where flux density S_{lin} is in Jy, and time t is MJD

in days. Fitting model light curves to the data with the slope removed then requires the following parameters to be estimated: (i) the unlensed flux densities and angular sizes of the lensed components, (ii) the location and orientation of the source trajectory over the magnification pattern, (iii) the Einstein crossing time, t_{E}, of the source components, and (iv) the flux density of source components that are not being lensed, assumed to be time-invariant. For simplicity, we assume that (i) all source components move at the same transverse speed along a north–south trajectory though the magnification pattern, and (ii) the source components have a bivariate Gaussian brightness profile with parameter $[\theta_s^x, \theta_s^y]$. We fit the cupid's bow lens with $\theta_s^x = \theta_s^y$, and the barbed arrow lens with $\theta_s^x > \theta_x^y$. Since the source size must be finite, we truncated the source brightness profile at $\pm 2\theta_s$.

Appendix C
Possible Evidence for More Extended Fold Caustic Patterns

The basic unit of symmetry we are exploring is the year-long U-shaped feature seen in 2009 and again in 2014 (Figure 1). However, there is possibly another symmetry evident in these data, namely the small peak near MJD 54466+1519, which is very close to the midpoint between the two peaks that straddle the small peak near MJD 54466+1519 in Figure 11, and are at MJD 54466+742.5±3.9 and MJD 54466+2295.7±1.8. These
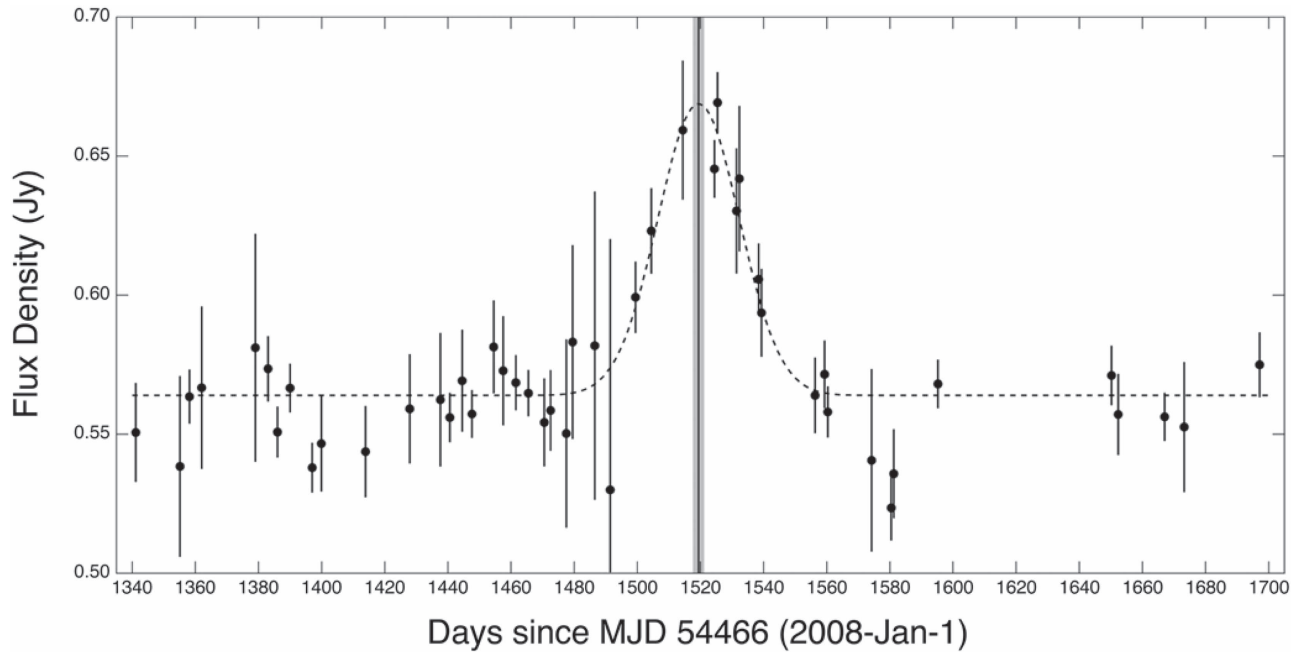
Figure 11. OVRO 15 GHz data for the one-year interval centered on the light curve peak near MJD 54466+1519. The position of the midpoint between the two adjacent peaks (not visible here) and the corresponding uncertainty are shown by the vertical gray bar. This agrees with the centroid of the Gaussian fit to the central peak (dashed line) to remarkable precision (0.18%; see the text) and is possibly evidence for an extended caustic network.

locations were determined by fitting low-order polynomials separately to the rising and falling parts of the light curves. The midpoint between these two adjacent peaks is therefore at MJD 54466+1519.1±2.1. We have used the data shown in Figure 11 to determine the position of the central peak by fitting a Gaussian to the central ~1 years of data, and we find that the centroid of the small peak lies at MJD 54466+1519.4±1.8. The difference of just 0.3±2.8 days between these two numbers may be compared with the relatively large interval of 1553 days between the adjacent two peaks. The above 1σ uncertainty amounts to only 0.18% of the interval between the two peaks and may therefore indicate that the two U-shaped features observed in 2008 and 2014 are related by a larger symmetry and that there is in fact a larger caustic network than we have assumed in the main text. Our simple lens models do not offer an explanation for this small peak at MJD 54466+1519, but given the symmetries that proliferate in gravitational lensing we believe that it should not be ignored at this early stage of exploring the SAV phenomenon.

Appendix D
Chance Alignment Probability

Let there be N_f foreground galaxies to N_s background radio sources and assume both are randomly distributed. We want to compute the expected number of instances where a background source and a foreground galaxy are projected (by chance) to within an angle θ_{off} from one another. The fraction of sky within a radial distance θ_{off} from any of the N_f foreground galaxies is $\pi\theta_{off}^2 N_f/(4\pi)$. The expected number of chance alignments is therefore $N_f N_s \theta_{off}^2/4$. If, however, the population of N_s sources is drawn from a flux density-limited sample (such as the OVRO 40 m sample), then those in close alignment with a foreground galaxy will be overrepresented due to magnification by the putative millilenses. We assume an average milli-lensing magnification of $\mu = 10$ (see Figure 6). For an intrinsic

source-count power-law with slope of 1.5 (Euclidean value), the magnification bias factor is $B_\mu = 10^{1.5} \approx 30$. For the OVRO survey, we have $N_s = 981$, and the required alignment for J1415+1320 is $\theta_{off} = 13$ mas. Based on the fits to the Press−Schechter function of Tomczak et al. (2014), we estimate that there must be about $N_f = 2 \times 10^8$ halos above a mass of $10^9 M_\odot$ up to redshift $z = 0.5$ (putative redshift of J1415+1320). Hence the expected number of radio sources in our sample with the required alignment is $B_\mu N_f N_s \theta_{off}^2/4 \approx 0.006$. While this is a low value, we remind the reader that this is a case of a posteriori statistics, so the argument against the background source hypothesis is not compelling. If halos of 10^8 and $10^7 M_\odot$ are also considered as viable foreground systems, then the corresponding numbers of chance alignments are 0.03 and 0.2, respectively, although it is unclear if halos in this mass range will host the putative lenses.

References

Alcock, C., Akerlof, C. W., Allsman, R. A., et al. 1993, Natur, 365, 621
Alcock, C., Allsman, R. A., Alves, D. R., et al. 2000, ApJ, 542, 281
Aller, M. F., Aller, H. D., & Hughes, P. A. 2003, in ASP Conf. Ser. 300, Radio Astronomy at the Fringe, ed. J. A. Zensus, M. H. Cohen, & E. Ros (San Francisco, CA: ASP), 159
Baars, J. W. M., Genzel, R., Pauliny-Toth, I. I. K., & Witzel, A. 1977, A&A, 61, 99
Begelman, M. C., Blandford, R. D., & Rees, M. J. 1984, RvMP, 56, 255
Beichman, C. A., Neugebauer, G., Soifer, B. T., et al. 1981, Natur, 293, 711
Blandford, R., & Narayan, R. 1986, ApJ, 310, 568
Blandford, R. D., & Kovner, I. 1988, PhRvA, 38, 4028
Blandford, R. D., & Narayan, R. 1992, ARA&A, 30, 311
Brinkerink, C. D., Müller, C., Falcke, H., et al. 2016, MNRAS, 462, 1382
Carilli, C. L., Perlman, E. S., & Stocke, J. T. 1992, ApJL, 400, L13
Carr, B. 1994, ARA&A, 32, 531
Carr, B., Kühnel, F., & Sandstad, M. 2016, PhRvD, 94, 083504
Chang, K., & Refsdal, S. 1979, Natur, 282, 561
Cohen, R. D., Smith, H. E., Junkkarinen, V. T., & Burbidge, E. M. 1987, ApJ, 318, 577
Conway, J. E., Pearson, T. J., Readhead, A. C. S., et al. 1992, ApJ, 396, 62
Fassnacht, C. D., Pearson, T. J., Readhead, A. C. S., et al. 1999, ApJ, 527, 498

Fiedler, R. L., Dennison, B., Johnston, K. J., & Hewish, A. 1987, Natur, 326, 675
Gopal-Krishna, & Subramanian, K. 1991, Natur, 349, 766
Gopal-Krishna, & Subramanian, K. 1996, A&A, 315, 343
Gugliucci, N. E., Taylor, G. B., Peck, A. B., & Giroletti, M. 2005, ApJ, 622, 136
Gurwell, M. A., Peck, A. B., Hostler, S. R., Darrah, M. R., & Katz, C. A. 2007, in ASP Conf. Ser. 375, From Z-Machines to ALMA: (Sub) Millimeter Spectroscopy of Galaxies, ed. A. J. Baker et al. (San Francisco, CA: ASP), 234
Hartman, R. C., Bertsch, D. L., Bloom, S. D., et al. 1999, ApJS, 123, 79
Healey, S. E., Romani, R. W., Cotter, G., et al. 2008, ApJS, 175, 97
Hovatta, T., Nieppola, E., Tornikoski, M., et al. 2008, A&A, 485, 51
Johnson, M. D., Kovalev, Y. Y., Gwinn, C. R., et al. 2016, ApJL, 820, L10
Kellermann, K. I., Vermeulen, R. C., Zensus, J. A., & Cohen, M. H. 1998, AJ, 115, 1295
Kobayashi, S., & Zhang, B. 2003, ApJL, 582, L75
Lamer, G., Newsam, A. M., & McHardy, I. M. 1999, MNRAS, 309, 1085
Lazio, T. J. W., Waltman, E. B., Ghigo, F. D., et al. 2001, ApJS, 136, 265
Lister, M. L., Aller, M. F., Aller, H. D., et al. 2016, AJ, 152, 12
Lister, M. L., Cohen, M. H., Homan, D. C., et al. 2009, AJ, 138, 1874
Lorimer, D. R., Bailes, M., McLaughlin, M. A., Narkevic, D. J., & Crawford, F. 2007, Sci, 318, 777
Marscher, A. P., & Gear, W. K. 1985, ApJ, 298, 114
Marscher, A. P., & Jorstad, S. G. 2010, arXiv:1005.5551
Mattox, J. R., Hartman, R. C., & Reimer, O. 2001, ApJS, 135, 155
McHardy, I. M., Abraham, R. G., Crawford, C. S., et al. 1991, MNRAS, 249, 742
Muñoz, J. B., Kovetz, E. D., Dai, L., & Kamionkowski, M. 2016, PhRvL, 117, 091301
Myers, S. T., Jackson, N. J., Browne, I. W. A., et al. 2003, MNRAS, 341, 1

Nieppola, E., Hovatta, T., Tornikoski, M., et al. 2009, AJ, 137, 5022
Oke, J. B., Cohen, J. G., Carr, M., et al. 1995, PASP, 107, 375
Ostriker, J. P., & Vietri, M. 1985, Natur, 318, 446
Ostriker, J. P., & Vietri, M. 1990, Natur, 344, 45
Perlman, E. S., Carilli, C. L., Stocke, J. T., & Conway, J. 1996, AJ, 111, 1839
Perlman, E. S., Stocke, J. T., Carilli, C. L., et al. 2002, AJ, 124, 2401
Press, W. H., & Gunn, J. E. 1973, ApJ, 185, 397
Pushkarev, A. B., Kovalev, Y. Y., Lister, M. L., et al. 2013, A&A, 555, A80
Readhead, A. C. S. 1980, in IAU Symp. 92, Objects of High Redshift, ed. G. O. Abell & P. J. E. Peebles (Dordrecht: Reidel), 165
Readhead, A. C. S., Cohen, M. H., Pearson, T. J., & Wilkinson, P. N. 1978, Natur, 276, 768
Readhead, A. C. S., Taylor, G. B., Xu, W., et al. 1996, ApJ, 460, 612
Richards, J. L., Max-Moerbeck, W., Pavlidou, V., et al. 2011, ApJS, 194, 29
Schneider, P., Ehlers, J., & Falco, E. E. 1992, in Gravitational Lenses (Berlin: Springer), 112
Schneider, P., & Weiss, A. 1987, A&A, 171, 49
Schneider, P., & Weiss, A. 1992, A&A, 260, 1
Stickel, M., Fried, J. W., & Kuhr, H. 1988, A&A, 198, L13
Stocke, J. T., Wurtz, R., Wang, Q., Elston, R., & Jannuzi, B. T. 1992, ApJL, 400, L17
Subramanian, K., Chitre, S. M., & Narasimha, D. 1985, ApJ, 289, 37
Taylor, G. B., Readhead, A. C. S., & Pearson, T. J. 1996, ApJ, 463, 95
Teraesranta, H., Tornikoski, M., Mujunen, A., et al. 1998, A&AS, 132, 305
Tomczak, A. R., Quadri, R. F., Tran, K.-V. H., et al. 2014, ApJ, 783, 85
Vedantham, H. K., Readhead, A. C. S., Hovatta, T., et al. 2017, ApJ, 845, 90
Webb, J. R., Howard, E., Benítez, E., et al. 2000, AJ, 120, 41
Wilkinson, P. N., Henstock, D. R., Browne, I. W., et al. 2001, PhRvL, 86, 584
Wilkinson, P. N., Polatidis, A. G., Readhead, A. C. S., Xu, W., & Pearson, T. J. 1994, ApJL, 432, L87